

Towards a single step process to create high purity gold structures by electron beam induced deposition at room temperature

C Mansilla¹, S Mehendale, J J L Mulders and P H F Trompenaars

FEI Electron Optics, 5651 GG Eindhoven, The Netherlands

E-mail: c.mansilla.sanchez@gmail.com

Received 8 April 2016, revised 2 July 2016

Accepted for publication 18 July 2016


Published 6 September 2016



CrossMark

Abstract

Highly pure metallic structures can be deposited by electron beam induced deposition and they have many important applications in different fields. The organo-metallic precursor is decomposed and deposited under the electron beam, and typically it is purified with post-irradiation in presence of O₂. However, this approach limits the purification to the surface of the deposit. Therefore, ‘*in situ*’ purification during deposition using simultaneous flows of both O₂ and precursor in parallel with two gas injector needles has been tested and verified. To simplify the practical arrangements, a special concentric nozzle has been designed allowing deposition and purification performed together in a single step. With this new device metallic structures with high purity can be obtained more easily, while there is no limit on the height of the structures within a practical time frame. In this work, we summarize the first results obtained for ‘*in situ*’ Au purification using this concentric nozzle, which is described in more detail, including flow simulations. The operational parameter space is explored in order to optimize the shape as well as the purity of the deposits, which are evaluated through scanning electron microscope and energy dispersive x-ray spectroscopy measurements, respectively. The observed variations are interpreted in relation to other variables, such as the deposition yield. The resistivity of purified lines is also measured, and the influence of additional post treatments as a last purification step is studied.

 Online supplementary data available from stacks.iop.org/NANO/27/415301/mmedia

Keywords: concentric nozzle, Au deposit, electron beam induced deposition, organo-metallic precursor, O₂ purification, nanofabrication

1. Introduction

Electron beam induced deposition (EBID) is a nanofabrication technique in which an electron beam induces the local dissociation of absorbed precursor molecules [1–3]. As a consequence, the solid fragment stays on the surface and the volatile fragment is pumped out. The balance between precursor molecules on the surface and available electrons, denoted as precursor working regime, can influence growth rates, deposit shapes and composition [4].

Au is a material which has potential for nanotechnological applications; in opto-electronics, for example, for the fabrication of plasmonic structures for manipulation of light, using gold antennas at sub-wavelength dimensions. In biotechnology and life sciences it can be used as sensor and lab-on-chip architectures due to its compatibility and affinity to biological molecules, and for nanowire contacting Au has one of the lowest resistivities of all metals [5–7].

A commonly used Au organometallic precursor is dimethyl gold acetylacetonate [Me₂Au-(acac)], which has a high potential to be applied in these fields [3, 8, 9]. However, this precursor leads to carbon rich EBID structures with only 10–15 at% Au with a very high resistivity of 10⁸ μΩ cm [10]

¹ Present address: Center of Physics of University of Minho, Campus de Azurem 4800-058, Guimaraes, Portugal.

as compared to that of the pure bulk Au at $2.3 \mu\Omega \text{ cm}$ [11]. The main technological problem for wider application of Au deposits in EBID is the low degree of purity of the deposits [5, 12].

Riazanova *et al* [7] summarize the different purification strategies in seven groups: post-annealing of deposited structures [3, 8], deposition onto heated substrates [13, 14], gas [15, 16] or water-assisted [17] EBID, EBID in ultra-high vacuum [18, 19], deposition from carbon-free precursor or aqueous solutions [20], variation of deposition parameters [3, 21], and post-treatment of deposited structures [9, 10, 17, 22–24]. Belic *et al* demonstrated the deposition of Au pillars of high purity with appropriate electron curing and O_2 post-treatment [12]. In addition, low-resistivity deposits have been achieved by Mehendale *et al* [6] by electron beam post-irradiation under oxygen.

Therefore, the use of O_2 simultaneously with the electron beam and the precursor appears as a very promising approach to improve the purity of the deposits in one step, which would also simplify its application in practice. Conventionally, the volatile precursor molecules are introduced into the microscope through a needle, near the desired deposition spot on the substrate. Then, the deposit can be purified with post-irradiation in presence of O_2 , or the deposition can take place using both flows in parallel using two needles. A special concentric double nozzle device has been designed allowing deposition and purification performed together in a single step. With this new device, metallic structures with high purity can be obtained more easily, as demonstrated previously for Pt depositions [25].

The aim of the present study is to evaluate the gold purity of the deposits by optimizing the deposition parameters using the new concentric double nozzle. First, we show deposits grown by the traditional way and post-treated afterwards with O_2 . Next, we introduce the deposits grown with the new device using different deposition parameters. On the basis of the experimental finding and guided by an expanded gas flow simulation model, we select the best conditions to prepare electrical contacts and measure their electrical response. The degree of improvement reached with the concentric-nozzle approach is evaluated by comparison with a deposit prepared without O_2 in the same setup.

2. Materials and methods

The depositions were performed in a FEI Helios Nanolab 660 dual beam system with a base pressure of $\sim 3.0 \times 10^{-6}$ mbar. Si wafers with a native oxide layer of ~ 3 nm were used as substrates, except for electrical measurements, where SiO_2/Si chips coated with pre-patterned 200 nm Au structures were employed. The precursor used for Au deposition was the conventional organo-metallic dimethylgold-acetylacetonate ($\text{Me}_2\text{Au}(\text{acac})$). Depositions were carried out at room temperature. Oxygen was introduced together with the precursor using a new concentric nozzle, with internal diameters 150 and 670 μm , which was located over the substrate at a nozzle-to-sample height below 700 μm . To find the

conditions for an optimized deposition, different parameters have been studied, such as the height between the sample surface and the nozzle, beam voltage and current, deposition time, dwell time, refresh time, spot overlap, electron dose and resulting O_2 chamber pressure.

The chemical composition of the deposits was evaluated by energy dispersive x-ray spectroscopy (EDX) (Oxford instruments, model X-max 80), using a beam energy of 5 kV and currents of 0.7 or 1.3 nA. Due to the overlap of C–K (280 eV) and Au–N x-ray lines (244 and 265 eV), the area ratio of the C–K line to the Au–M line (C/Au) was used to evaluate the purity of the deposit. Note that the EDX systems mostly ignore the Au–N line and identify it wrongly as C–K. The C/Au ratio is neither at% or wt% but a ratio of the net peak intensity only, so not divided by the pure element intensity to obtain the K-ratio. It is a signal ratio prior to any correction for excitation, absorption and fluorescence. To ensure a meaningful evaluation, a pure gold reference was also measured. All the measurements have been carried out in the same geometrical arrangement.

The measurements were performed using an effective spot size of 90 nm to prevent spot burns. The maximum penetration depth of electrons in the deposits has been estimated through simulations performed using CASINO software [26]. The microstructure of the deposits has been measured by top view and cross-section scanning electron microscope (SEM) images acquired at 2 or 5 kV. Cross sections have been prepared using a Ga^+ ion gun operating at 30 kV and 24 pA. Deposits have been protected with a ~ 250 nm thick Pt layer prior to Ga^+ bombardment.

Resistivity was evaluated from $V(I)$ curves acquired using four-points probe measurements (Keithley source meter 2614B, see image in the online supplementary material). The current was varied while the voltage was measured. The values of resistance were obtained from the slope of the I – V curve (see an example in online supplementary material). In this typical structure the resistance can be measured without any influence of the contact resistance, and the resistivity can be calculated using the area of the cross section measured by SEM. The nominal dimensions of the lines were 11 μm length and 0.10 μm width. The height of the lines was controlled through the deposition time.

3. Results and discussion

3.1. Post-treatment versus 'in situ' purification

Figure 1 shows three deposits prepared at three incremental deposition times (5, 10 and 20 min). For each case, three different oxygen post-treatment times are carried out (from right to left in each image). The duration of the O_2 treatments is also depicted on the figure (top row). Vertical dashed lines on the top two rows indicate the limits among the different treated regions. By comparison of the untreated deposits (time 0), it can be seen that longer deposition times lead to approx. proportional thicker deposits (thicknesses of 85, 160 and 300 nm). In all cases, the post-treatments lead to the

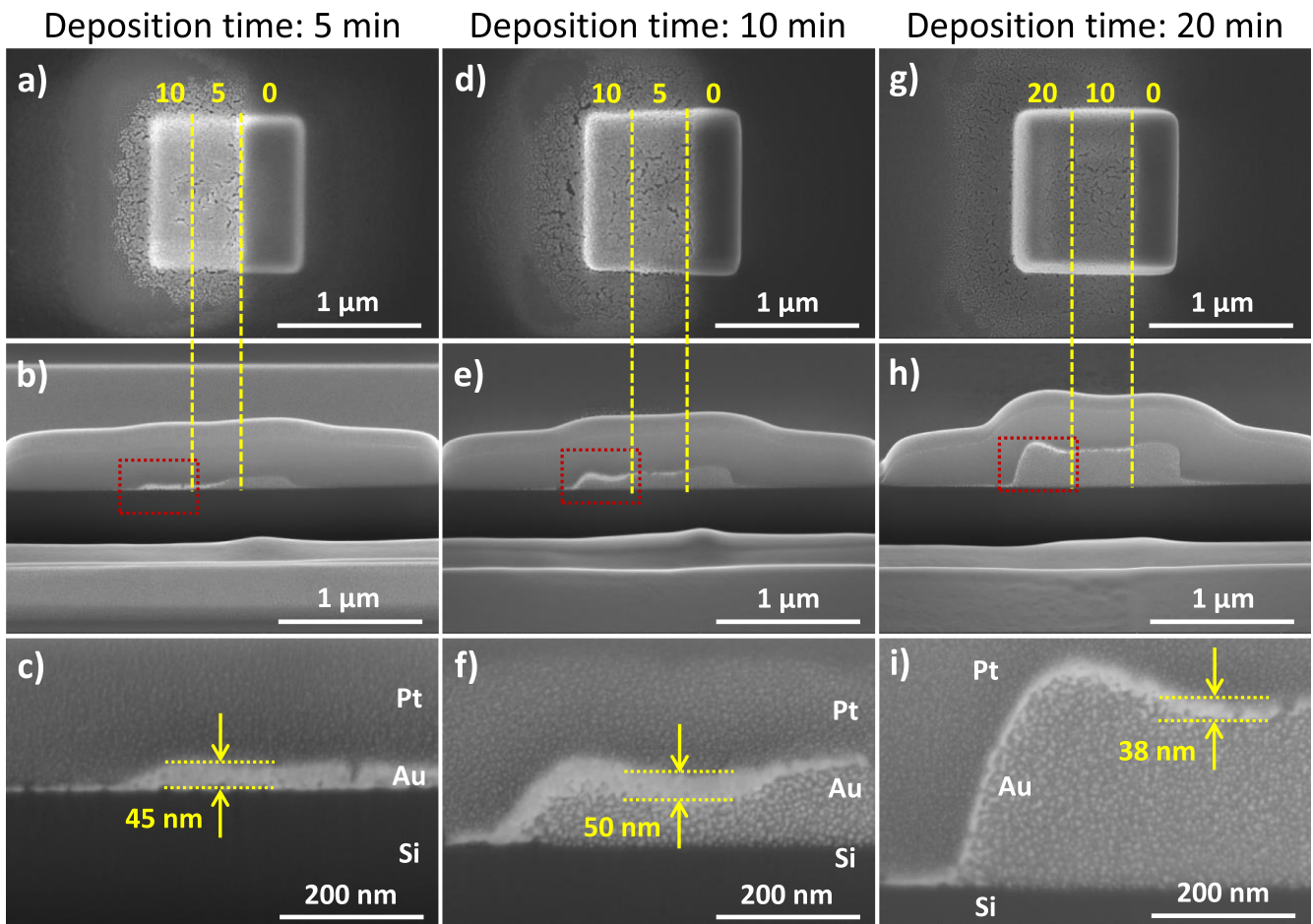


Figure 1. SEM images of deposits prepared at different deposition times and post-treated with O_2 (the treatment time is indicated in each figure). Top row: top views. Middle row: cross-sections. Bottom row: detailed cross-sections of the regions after longer treatment times (indicated with red rectangles in the middle row).

reduction of the total thickness of the deposits and the appearance of a bright region at the top (see middle row in figure 1). Thicker regions are obtained at longer post-treatment times. This brighter region can also be appreciated in the top view, and better for the thinnest deposit (figure 1(a), left). The halo around is present in all the deposits and it is more evident after the post-treatments (see regions near the deposits in the cross sections in the middle and bottom rows), but it is not visible on the top view of the thickest deposit. In the bottom row, a detailed view of the regions with longer treatments is shown, which correspond with the areas indicated by red rectangles in the middle row. It can be seen that the deposits are formed by bright grains (Au) embedded in a dark matrix (carbon). Only the top part of the deposits is affected by the post-treatments, where the formation of a bright Au surface is observed (see figures 1(f) and (i)). Only in the case of the thinnest deposit a purification over the full height is achieved after 10 min of post-treatment (figure 1(c)). From these images, it can be concluded that the maximum thickness of the purified region is around 50 nm (figure 1(f)) and values in similar range are seen in figures 1(c) and (i). The maximum purification thickness can be calculated to be ca. 100 nm in figure 1(e), considering the difference between

the as-deposited region (post-treatment time 0) and the area purified during 10 min, excluding the thickness of the purified layer (ca. 50 nm). This value is in good agreement with the original thickness of the film deposited with lower time (85 nm), which is reduced to a final thickness of ca. 45 nm.

The values of C/Au ratios measured by EDX for the deposits and post-treatments depicted in figure 1 are included in figure 2(a). The C/Au ratio for all untreated deposits is similar (around 0.45), and their purity increases as a consequence of the post-treatments, as may be expected (i.e. lower C/Au ratios). It is observed that a steady state is obtained for the thinnest deposit at $C/Au = 0.05$, which is the value of pure gold. The other two deposits are also purified by the post-treatment, but the purification rate is slower for thicker deposits. In fact, a ratio indicating high purity is not reached for the thickest sample, even after 20 min of post-treatment. This effect can only be explained by assuming that a certain amount of oxygen is absorbed into the porous deposition during the post-treatment. The density of absorbed oxygen will be higher in case of a thinner deposition layer, leading to a more rapid purification. The presence of absorbed or entrapped oxygen in the deposition layer was also described by Villamor *et al* [25]. Nevertheless, it is worth

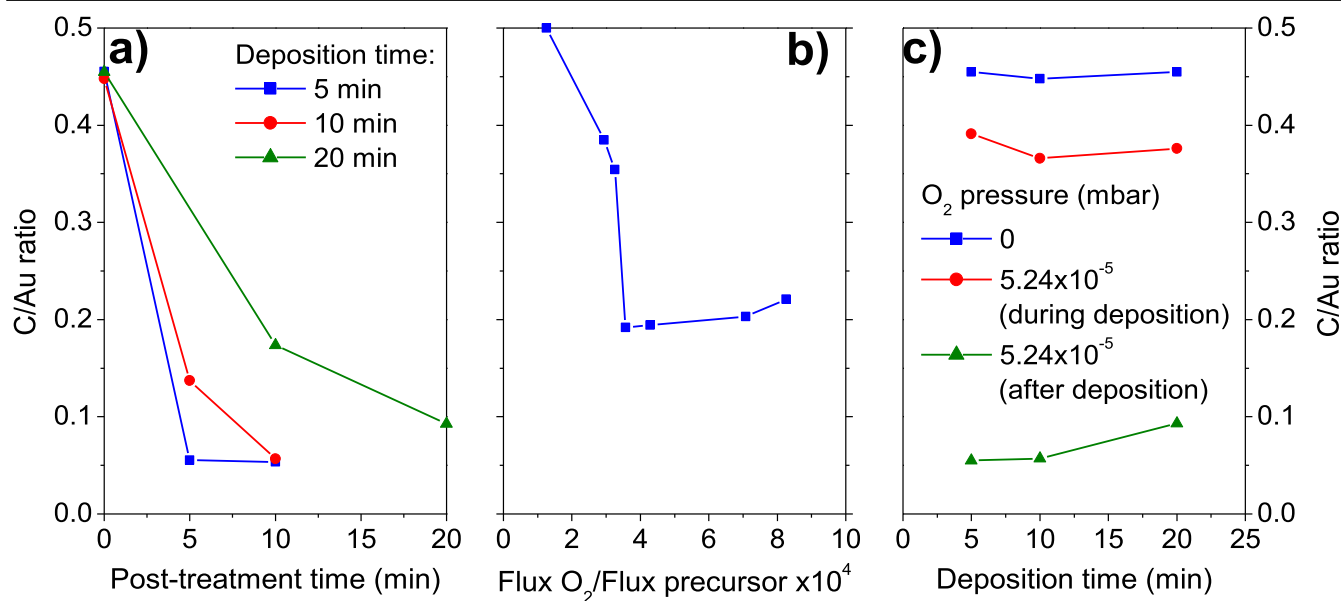


Figure 2. Influence of different ways of O₂ exposure on the C/Au ratio. (a) Post-treatment with the three conditions and exposures shown in figure 1. (b) Simultaneous purification using two independent nozzles for O₂ and the Au precursor. (c) Simultaneous purification using the concentric nozzle, with different deposition times and O₂ conditions. The results obtained in similar conditions with post-treatment and without purification are also depicted for comparison.

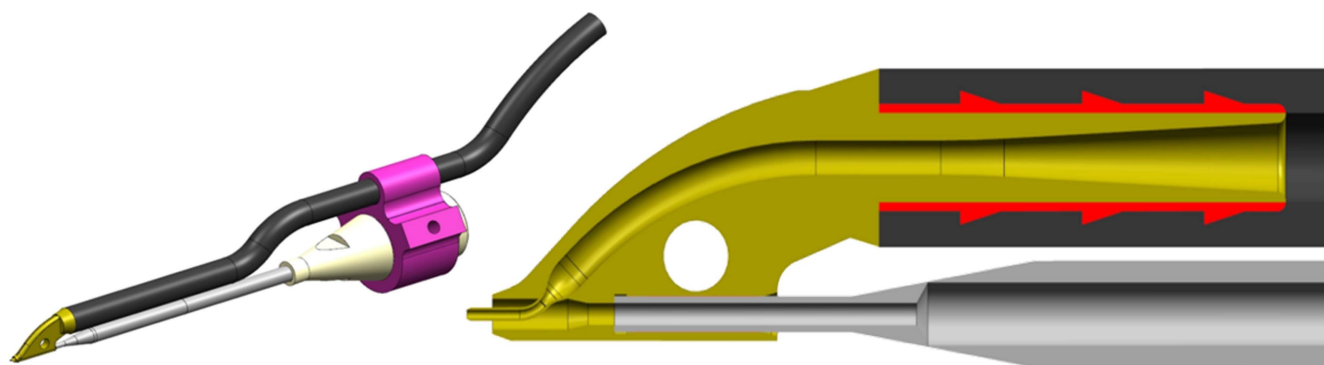


Figure 3. Drawing of a dual concentric nozzle. Left: as mounted on a standard GIS needle. Right: detailed cross section, showing the slight protrusion of the inner nozzle. The inner nozzle provides the high flux O₂ while the outer nozzle provides the low flux precursor. (Patent pending.)

mentioning that under the selected conditions EDX only measures the top part of the deposit (around 45–50 nm), since the case shown in figure 1(f) (i.e. the sample deposited and post-treated during 10 min) is not totally purified, but it reaches the value of C/Au of pure gold. This ‘detection thickness’ of EDX is in agreement with the maximum penetration depth of electrons in pure gold under these conditions, according to CASINO simulations.

Therefore, the post-treatment approach is valid for the purification of deposits only if they are thin enough (<100 nm). In case of thicker deposits, the purification takes place only in the upper layers of the sample and the densification impedes the advance of the purification process to deeper regions. These results are indeed quite similar to what observed for Pt [27] and Au [6]. In this latter case, a multi-layer deposition was made with a final resistivity of 17 $\mu\Omega$ cm. To speed up the process and avoid the complexity of a multi-layer approach, the obvious next step is to do both

tasks (deposition and purification) simultaneously. This was done using two separate nozzles, a standard nozzle for precursor supply, and a smaller diameter nozzle for high flux O₂ supply. In a single step process, the beam current and exposure time are the same for ‘deposition’ and ‘purification’. Since the O₂ flux was set to a maximum value (limited by the microscopes vacuum system and the size and distance of the nozzle), the main variable was the precursor flux, which was turned down by retracting the nozzle in small increments. The results are depicted in figure 2(b). The C/Au ratio reveals an incomplete purification, and large halos are observed (not shown). In a similar approach for Pt deposition from MeCpPtMe₃, a high purity deposition (>95 at%) for Pt could be obtained [25]. Nevertheless, a requirement for this process to be effective is a flux of O₂ that is few orders of magnitude larger than the flux of precursor (see x axis in figure 2(b)).

To accommodate this simultaneous supply a dual nozzle has been designed, providing a single device that delivers two

gas flows. The main advantage of such a device is the ease of use, preventing a more complex two-nozzle set up and its required mutual alignment, which is critical for the process to be effective. The dual nozzle has been realized as an add-on nozzle to an existing gas injector system (GIS) and is schematically shown in figure 3. The nozzle provides a concentric system with an internal tube that is slightly longer than the concentric outer tube. The inner tube with typical diameter of $150\ \mu\text{m}$ provides the oxygen flux, while the external concentric tube with inner diameter $670\ \mu\text{m}$ provides the precursor flux. In this way, mixing only occurs at the space above the sample, while back streaming is minimized. This system has also successfully been used for 'in situ' one step purification of Pt [25].

To quantify both the flux of O_2 and of the precursor, an existing GIS simulator model [28] was adapted to accommodate the new geometry. In this way, it is possible to run simulations on the applied nozzle geometry and study the influence of variations of dimensions such as tube diameters and protrusion length of the inner tube. When developing this model for the new geometry, both the inner and outer tubes are calculated individually assuming molecular flow. For both tubes the flux dilution into vacuum is calculated as a function of axial distance and distance to the nozzle. The model adaptation also provides a way to plot the ratio of the absolute fluxes of precursor and O_2 ; this is achieved by adding the vacuum system parameters such as effective pump speed at $70\ \text{l s}^{-1}$ and pressure increase for each individual tube. These data and the area cross-section for each tube result in an absolute number for the average flux at the output surface of each tube. The numerical model provides normalized data as a fraction of the average output flux; by recalculation to the absolute numbers, the real flux ratio between precursor and oxygen can be plotted as a function of position. By adding the sample and the electron beam impact point the flux ratio of the process is known.

Applying the model, it was shown surprisingly that the outer tube flux peaks at the outer edge and not in the middle of the tube opening. This can be explained by the fact that, of course, the inner tube surface area is much smaller than the outer tube surface area and hence molecular hits on the outer surface are more frequent than inner tube hits. An example of such an outer tube distribution is shown in figure 4. Using the applied geometry in the experiments, the actual dimension of the nozzle and the position of the sample and the beam impact point, it is possible to calculate the mix ratio at that point. Or reverse, it is possible once the optimal mix ratio is known from experiments, to map the points in space where this ratio is obtained. An example of this is shown in figure 4: for a required typical mix ratio of 10^4 , it is possible to determine where these positions can be found and hence, where to put the sample. The calculated map showing both the distribution of the oxygen and the positions where the mix ratio is 10^4 is given in figure 4. Note that the O_2 distribution is shown as a fraction of the averaged output flux and the red points present the locations where the mix ratio is 10^4 .

Experiments described in this paper were done with the sample at the location indicated by the red dots, so at one of

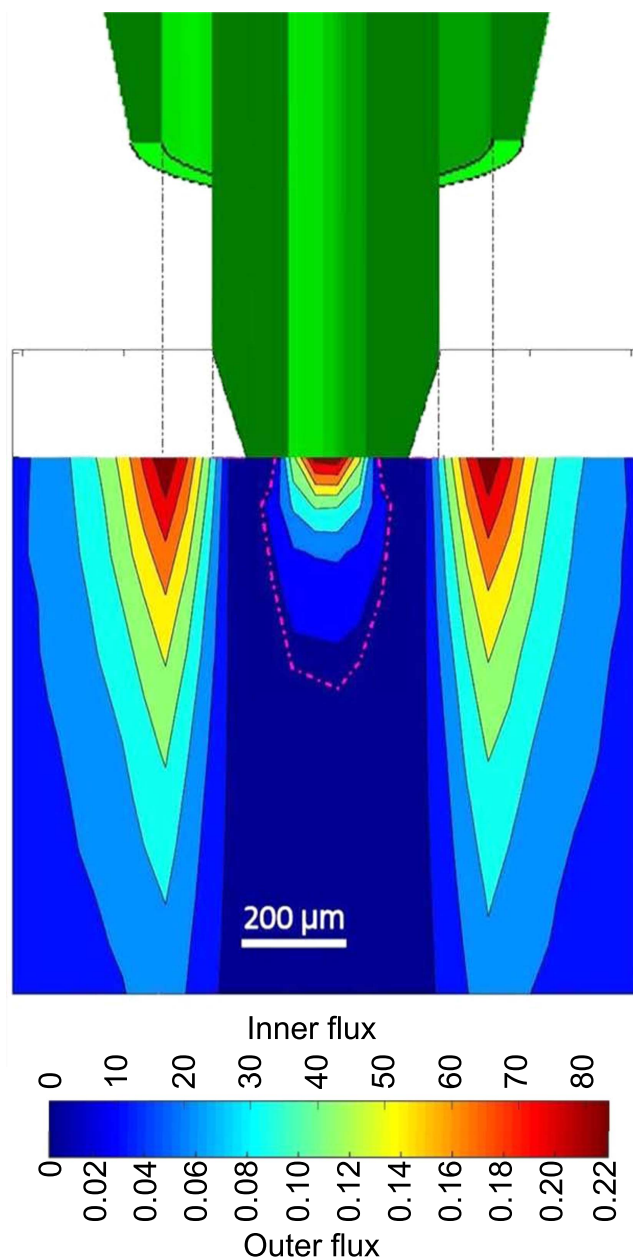


Figure 4. Outer and inner tube flux distribution obtained from GIS simulations [16].

the plotted mix ratio positions shown in figure 4. However, it is worth mentioning that the precursor supply may take place via surface diffusion as well, which is not considered in this model. Therefore, predictions based on the simulations may have a limited value, and fail to distinguish between the behavior of different precursors.

The first results of the new GIS system for Au deposits prepared at different deposition times are compared in figure 2(c) with samples with no O_2 exposure (which correspond to the deposits at post-treatment time 0 in figure 2(a)). In addition, samples that have been deposited and post-treated with O_2 for the same time (i.e. 5 + 5, 10 + 10 and 20 + 20 in figure 2(a)) are also included, which show a clear C/Au reduction with respect to the corresponding non-exposed

ones, as explained before. The samples that have been exposed to O_2 during the deposition using the concentric double nozzle represent an intermediate situation between these series. This is because they have been deposited for the same time than the samples of the other two series, but they have been exposed to O_2 simultaneously for the same times used in the post-treated series. It can be seen that these samples are also purified (lower C/Au than the non-exposed samples), although the results are not as good as the post-treated ones. Therefore, the deposition using a concentric double nozzle providing O_2 together with the organo-metallic precursor may be helpful for one-step purification of Au films. Nevertheless, further optimization of the process is needed in order to move towards the results obtained with the oxygen post-treatment.

3.2. Concentric nozzle: optimization of parameters

Figure 5 shows the influence of the distance between the concentric double needle and the sample surface for three series of deposits prepared using different pressures of O_2 during deposition. The deposition yields show decreasing trends when the needle approaches the sample surface (figure 5(a)), which is likely caused by a ‘shadowing’ effect caused by the nozzle, in agreement with results observed by the gas flow simulations (not shown). These results suggest that the deposition process is controlled by the precursor under constant electron irradiation. Nevertheless, the yields obtained for samples prepared with O_2 during deposition are lower, indicating a removal of C due to purification. Such behavior can be better appreciated on the C/Au ratios measured by EDX (figure 5(b)). At large distances, the series show the same C/Au ratios as the values observed for the untreated samples, and also for the samples prepared simultaneously with O_2 shown in figure 2(c), since these latter deposits were prepared at $\sim 650 \mu\text{m}$. At shorter distances, the C/Au ratio of the series prepared without presence of O_2 increases, which is probably caused as an effect of the low thickness ($< 50 \text{ nm}$ of deposit) on the EDX measurements. In fact, exponential fittings were performed to deposition yield and C/Au ratio for the deposits prepared without O_2 (blue lines in figure 5), and both trends could be fitted with the same exponent. This means that the C/Au ratio varies at the same rate as the thickness of the deposits (note that deposition yield is directly proportional to thickness for constant electron dose). This observation is probably a consequence of the lines selected to monitor C and Au concentrations. The difference of energy is pretty large, and causes a difference of absorption coefficient larger than one order of magnitude [29]. This means that C signal is restricted to regions closer to the surface, since from deeper atoms is mostly absorbed. In contrast, the Au signal from the full region reaches the detector. As a consequence, when the thickness is reduced, the Au signal decreases more than the C signal, leading to increased C/Au ratios.

The other two series prepared with O_2 show lower C/Au ratios than the untreated series, indicating a clear effect of the

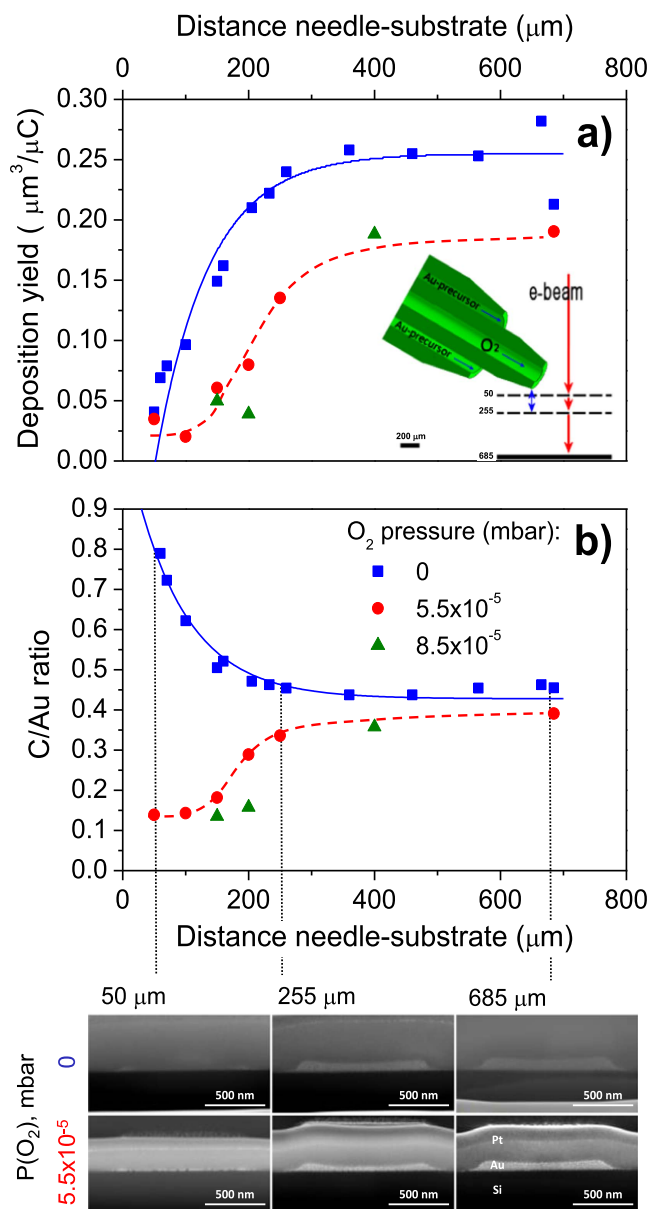


Figure 5. Influence of the needle-substrate distance and O_2 pressure during deposition on the C/Au ratio (a) and deposition yield (b). The blue continuous lines for the series without O_2 are exponential fittings with the same exponent. The dashed red lines are guides for the eye. A scheme of the geometric arrangement is included as an inset in (a). In the bottom, cross-section SEM images of some selected deposits at different needle-substrate distances.

purification. However, the values are closer at high distances, which indicates that the influence of O_2 is limited. In contrast, at lower distances the C/Au ratio decreases and separates from the untreated series, revealing a stronger effect of the O_2 . In fact, the shape of the C/Au trend resembles the one shown by the deposition yield. This indicates that a high degree of purification is correlated with a lower thickness of the deposit. Selected cross-section SEM images from the series without O_2 and at $P = 5.5 \times 10^{-5}$ mbar at three needle-surface distances (ca. 50, 255 and 685 μm) are also included in the bottom of figure 5. It can be seen that deposits prepared at shorter distances are thinner than those prepared at higher

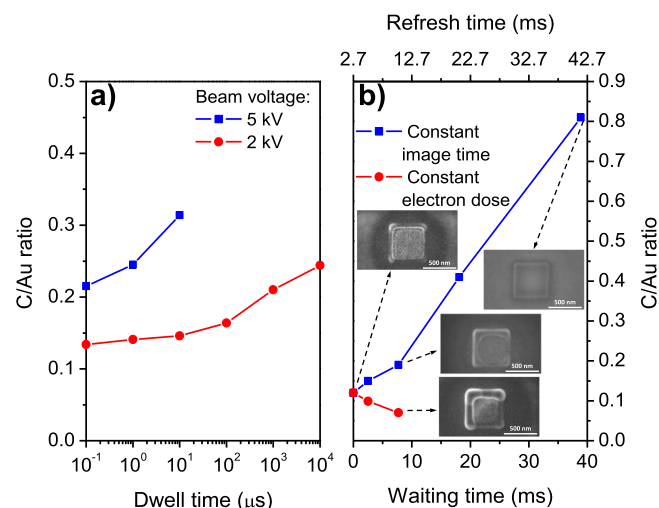


Figure 6. Influence of different beam parameters on the C/Au ratio of the deposits. (a) Deposition voltage and dwell time at constant electron dose. (b) Waiting time (see table 1). SEM pictures of selected deposits are also included in (b).

distances, and also show larger height differences between the center and the edges of the deposits. In addition, samples deposited with O₂ show more contrast and larger Au grains, as a consequence of the purification process. For further analyzes, values of ca. 200 μm and $P(O_2) = 8.5 \times 10^{-5}$ mbar are selected as optimal, since the yield is still high and the C/Au ratio is low.

Subsequent optimization of the purification process entails a fine tuning of the different beam parameters. A value of 0.67 nA was selected as a compromise between reasonable operation time and good purity. The effect of beam voltage and dwell time is illustrated in figure 6(a). In both series, the C/Au ratio decreases for shorter dwell times. In parallel, the deposition rates remain invariant (thickness about 15 and 55 nm for 2 and 5 keV, respectively), as expected for deposits prepared at constant image time and electron dose. The improvement of deposit purity in each series is probably a consequence of the higher number of frames that are used at lower dwell times, which leads to a much higher number of deposition-purification loops and probably higher entrapment/absorption of O₂ [25]. In addition, the operation at 2 kV appears better than at 5 kV. This is a direct consequence of the expected and observed much larger deposition rates at 5 kV (55 nm versus 15 nm at 2 kV), which reduce the efficiency of the purification process. Therefore, subsequent deposits are prepared at 2 kV and 1 μs, unless specified otherwise.

Figure 6(b) shows the influence of the waiting time of the beam on the C/Au ratio of two series of samples (details are summarized in table 1), including some selected top view SEM images. In the first series, the total image time is kept constant and therefore, the electron dose is higher at lower waiting times. As a consequence of the former, the thickness of the deposits remains quite stable around 25 nm, in agreement with a precursor-controlled process. As a consequence

of the latter, it is observed that the C/Au ratio reduces at shorter waiting times, but the shape of the deposit worsens. This is because larger amounts of electrons are available for purification, which causes larger deformations of the shape of the deposits. It is worth mentioning that these results are relevant, since the C/Au changes a lot for deposits with similar thickness, and reveals the importance of increasing the amount of available electrons in order to improve the purification process (while the thickness of the deposits remains more or less unaffected).

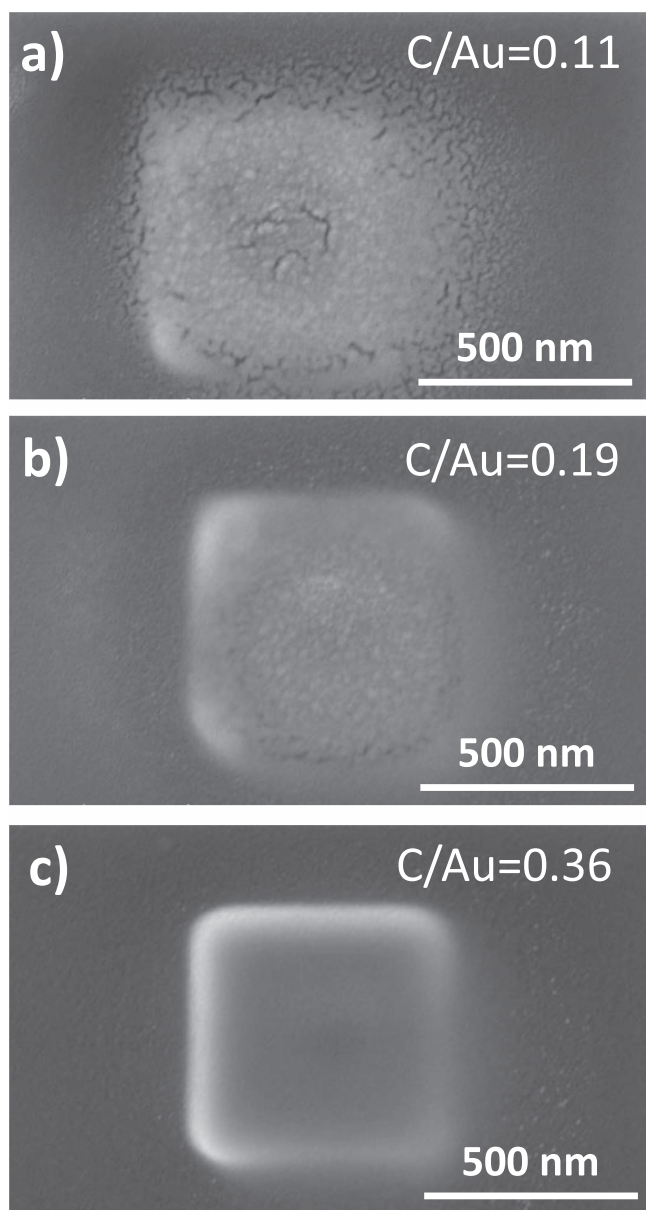
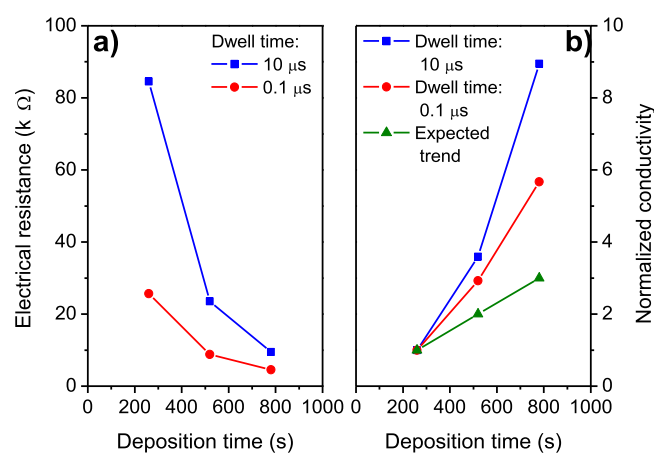
In the second case, the electron dose is kept constant by increasing the total image time in parallel to the waiting time, which causes the total image time to increase (see table 1). Therefore, the amount of available precursor increases, which leads to a clear increase of the thickness of the deposits from ca. 25 to 75 nm, confirming the precursor control of the deposition. In fact, these deposits correspond to those of the first series at the same waiting time, but with adapted number of frames (and image time) to reach a constant electron dose (table 1). In other words, they are prepared with the same image conditions but with higher thickness. This can be appreciated on the film grown at waiting time of 7.7 ms; the shape is the same, but the thickness is higher. Nevertheless, the C/Au ratio is lower. This is a consequence of the effect that was explained in figure 3 for samples deposited without O₂. When increasing the thickness of the deposit (which is the case here), the C/Au ratio can be reduced as a consequence of the progressive absorption of the C–K photons.

An alternative option to explore the variation of waiting time at constant electron dose (like in the preceding set of samples) consists on the modification of the dwell time, as indicated in table 1. Thus, increased dwell time leads to longer loop times. Since the refresh time of the image is kept constant, the waiting time is reduced, and therefore shorter total image times are needed. The number of frames is adjusted from one case to another to reach a constant electron dose. The result of these experiments are shown in figures 7(a)–(c). As expected, the thickness increases from ca. 20 to 110 nm for longer waiting times (i.e. shorter dwell times and longer image times, see table 1), in agreement with a precursor-controlled deposition process. In parallel, the C/Au ratio increases and the shape of the deposit gets better. These latter results are a consequence of lower purification that takes place at constant electron dose but higher thickness of the deposit.

Finally, three different spot overlaps (25%, 50% and 75%) have been studied on images prepared at constant electron dose (see online supplementary material). Images at high overlap have, for a given electron dose, a lower number of frames, and therefore the total image time is lower. It was observed that larger overlaps produces better purity, although the shape of the deposits gets worse. These results are a consequence of the lower thickness of the deposit and higher purification with O₂, which confirms the precursor-control of the deposition and the better purification in situations with higher electron/precursor ratios.

Table 1. Synthesis condition of deposits where the influence of waiting time has been explored (figures 6(b) and 7).

Dwell time (μs)	Loop time (ms)	Waiting time (ms)	Refresh time (ms)	Number of frames	Total image time (min)	Total electron dose ($\text{nC } \mu\text{m}^{-2}$)
1	2.7	38.9	41.6	7203	5	52
1	2.7	18.1	20.8	14 459	5	105
1	2.7	7.7	10.4	28 846	5	209
1	2.7	2.5	5.2	58 275	5	422
1	2.7	0	2.7	115 385	5	835
1	2.7	2.5	5.2	115 385	10	835
1	2.7	7.7	10.4	115 385	20	835
10	27.0	16.2	43.2	11 229	8.1	813
7.5	20.3	22.9	43.2	14 972	10.8	815
5	13.8	29.4	43.2	22 458	16.1	829

**Figure 7.** SEM pictures of deposits prepared with different dwell times and constant refresh times. (a) 10 μs ; (b) 7.5 μs ; (c) 5 μs . See table 1 for details.**Figure 8.** Effect of dwell time and deposition time on the electrical properties of the deposits. (a) Resistance. (b) Normalized conductivity.

3.3. Electrical performance and influence of post-treatments

After the screening of the deposition parameters, the electrical response of two lines has been evaluated. For each case, three different thicknesses have been tested. In all cases the $V(I)$ curves are linear (see example in online supplementary material), indicating ohmic behavior. From the slopes of the plots the resistances of the structures can be obtained. These results are summarized in figure 8. We can see that the line prepared with shorter dwell time shows better properties, in agreement with the improvement of purity shown in figure 6(a). Furthermore, in both cases the resistance decreases with the thickness of the deposit. Nevertheless, the enhancement of the electrical response cannot be fully attributed to a larger cross-section of the line, as illustrated in figure 8(b). In this graph the conductivity of the deposits has been normalized to the values of the initial (thinnest) one, and it is compared with the expected growth considering the incremental size of the line with deposition time. It is clearly observed that the conductivity increases beyond the expectations, and more for the line with worse properties (dwell time 10 μs). Moreover, the improvement increases from the second point to the third in both series. These effects can be attributed to a better

Table 2. Characteristics of lines with different preparation and post/treatment condition.

In figure 9	Treatment	C/Au ratio	R (Ω)	ρ ($\mu\Omega$ cm)
a	Deposited without O_2	0.45	101 440	3.1×10^4
b	Deposited with O_2	0.1	29 552	5.3×10^3
c	Case b, with e^- irradiation	0.083	189	1.7×10^1
d	Case c, with e^- irradiation under O_2	0.062	50	4.8
e	Case b, with e^- irradiation under O_2	0.068	427	3.5×10^1
f	Case e, with e^- irradiation	0.087	—	—

connectivity among the gold grains for larger thickness of the deposit. In general, the resistivity of the line with optimized condition is ten times lower than a line deposited without O_2 under similar conditions in the same equipment, and much better (4–5 orders of magnitude) than the values reported in literature [10].

In the final part of this manuscript we briefly evaluate the influence of different additional post-treatments on a thin line with optimal properties (thick lines are only treated on the outer surface, as shown in figures 1 and 2). The aim of this study is to evaluate critically the degree of optimization that can be achieved using the concentric needle, and how much can be improved from that value with the traditional post-treatments; in other words to obtain the ultimate low resistivity. The characteristics of the different post-treatments are summarized in table 2, and the microstructures of the cross-sections are depicted in figure 9. First of all we can see that the cross-section of the line prepared without O_2 is larger (figure 9(a)) than the line prepared with O_2 during the deposition (figure 9(b)). In addition, the purity and the electrical response are worse due to the higher presence of C. It is observed that the beam irradiation under O_2 leads to the largest modification in the microstructure (figures 9(c)–(d) and (b)–(e)). Hence, the Au grains embedded in a carbonaceous matrix are turned into a dense Au-rich structure. In comparison, the electron irradiation without O_2 causes a minor structural change, although a better interconnectivity could be inferred in top-view images (see online supplementary material). In general all these post-treatments lead to sequential improvements of the purity and electrical response (table 2); the resistivity improves between two and three orders of magnitude, reaching values close to pure Au bulk resistivity, $2.27 \mu\Omega$ cm [11]. Nevertheless, it is worth mentioning that just an electron post-treatment after the deposition with O_2 (figure 9(c)) already reaches a value of $17 \mu\Omega$ cm, which can be enough for many applications.

It is worth mentioning that the ‘*in situ*’ approach has been also employed in the purification of Pt, with a larger reduction of resistivity [25]. This difference is probably related to the chemistry of the precursor; in the present case it seems that a larger amount of electrons during the process would have led to higher purity, probably closer to what was observed in Pt. In other words, further optimization for purified Au deposits could be possible.

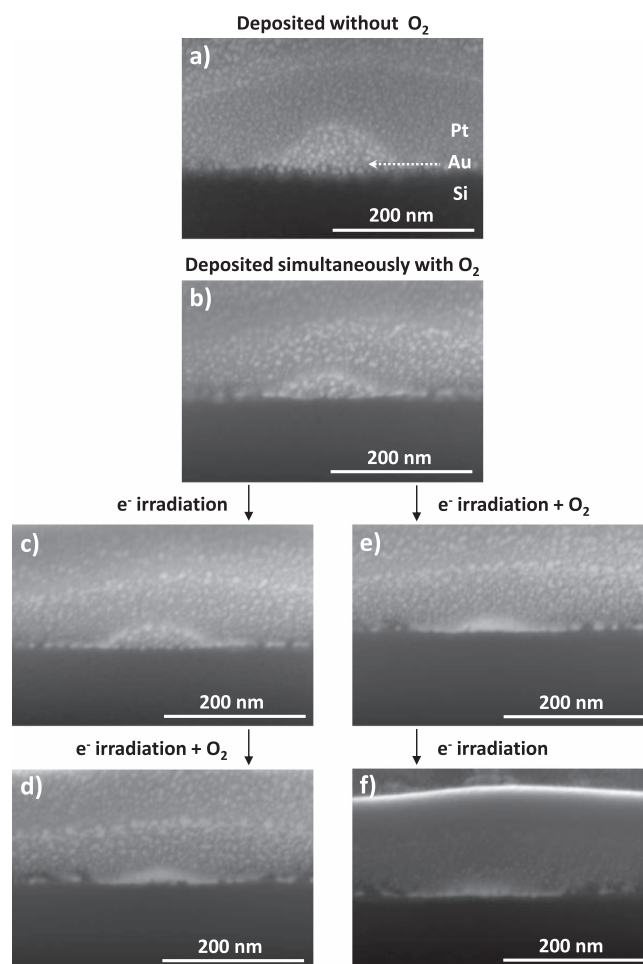


Figure 9. Influence of different post treatments on the microstructure of the deposited lines. (a) Without O_2 . (b) With Au and O_2 simultaneously in a single step using the concentric nozzle. (c) Condition b followed by electron beam irradiation. (d) Condition c followed by electron beam irradiation under O_2 . (e) Condition b followed by electron beam irradiation under O_2 . (f) Condition e followed by electron beam irradiation. See table 2 for details.

4. Conclusions

In this work we describe the use of a new concentric double nozzle that allows deposition of metallic deposits using simultaneous supply of the organo-metallic precursor and O_2 under electron beam irradiation. The advantage of this approach is a simplified practical operation: it is better adapted to experimental feasibility constraints, and it is not

limited to the surface-bound purification of the conventional post-treatments.

The most relevant deposition parameters have been evaluated and optimized using the C/Au ratio and SEM to characterize the purity and (micro)structure of the deposits. It has been concluded that, in this experimental conditions, the deposition process is controlled by the precursor. In addition, the purification is better at higher electron dose. It is also observed that a shorter dwell time (keeping the other parameters invariant) leads to a better purity of the deposit, probably because of the higher number of frames. In general, the shape of the deposit worsens when the purification is higher.

Finally, the electrical properties have been evaluated through four-point measurements, and compared with a reference that has not been post-treated prepared in the same equipment. An enhancement of the purity of the deposit and a clear reduction of the resistivity by an order of magnitude against deposits prepared in the same equipment, and 4–5 orders versus results in literature, has been achieved.

Acknowledgments

EMPA is acknowledged for providing the original code for the GIS simulator model, which was extended by Stan de Muijnck (TU Delft) with the new geometry. Pleun Dona (FEI) is acknowledged for helping in the design of the concentric nozzle and in getting a working prototype. Patricia Peinado is also acknowledged for help on experimental activities. This work was supported by NanoNextNL program, a Dutch national research and technology program for micro- and nano-technology.

References

- [1] Utke I, Moshkalev S and Russell P 2012 *Nanofabrication Using Focused Ion and Electron Beams: Principles and Applications* (Oxford; New York: Oxford University Press)
- [2] van Dorp W F and Hagen C W 2008 A critical literature review of focused electron beam induced deposition *J. Appl. Phys.* **104** 81301
- [3] Botman A, Mulders J J L and Hagen C W 2009 Creating pure nanostructures from electron-beam-induced deposition using purification techniques: a technology perspective *Nanotechnology* **20** 372001
- [4] Arnold G, Timilsina R, Fowlkes J, Orthacker A, Kothleitner G, Rack P D and Plank H 2014 Fundamental resolution limits during electron-induced direct-write synthesis *ACS Appl. Mater. Interfaces* **6** 7380–7
- [5] van Dorp W F, Wu X, Mulders J J L, Harder S, Rudolf P and De Hosson J T M 2014 Gold complexes for focused-electron-beam-induced deposition *Langmuir* **30** 12097–105
- [6] Mehendale S, Mulders J J L and Trompenaars P H F 2015 Purification of Au EBID structures by electron beam post-irradiation under oxygen flux at room temperature *Microelectron. Eng.* **141** 207–10
- [7] Riazanova A V, Rikers Y G M, Mulders J J L and Belova L M 2012 Pattern shape control for heat treatment purification of electron-beam-induced deposition of gold from the Me₂Au(acac) precursor *Langmuir* **28** 6185–91
- [8] Graells S, Alcubilla R, Badenes G and Quidant R 2007 Growth of plasmonic gold nanostructures by electron beam induced deposition *Appl. Phys. Lett.* **91** 121112
- [9] Höflich K, Yang R B, Berger A, Leuchs G and Christiansen S 2011 The direct writing of plasmonic gold nanostructures by electron-beam-induced deposition *Adv. Mater.* **23** 2657–61
- [10] Botman A, Mulders J J L, Weemaes R and Mentink S 2006 Purification of platinum and gold structures after electron-beam-induced deposition *Nanotechnology* **17** 3779–85
- [11] Chemical Rubber Company and Weast R C 1986 *CRC Handbook of Chemistry and Physics* (Boca Raton, FL: CRC Press)
- [12] Belić D, Shawrav M M, Gavagnin M, Stöger-Pollach M, Wanzenboeck H D and Bertagnolli E 2015 Direct-write deposition and focused-electron-beam-induced purification of gold nanostructures *ACS Appl. Mater. Interfaces* **7** 2467–79
- [13] Koops H W P 1996 Conductive dots, wires, and supertips for field electron emitters produced by electron-beam induced deposition on samples having increased temperature *J. Vac. Sci. Technol. B* **14** 4105
- [14] Mulders J J L, Belova L M and Riazanova A 2011 Electron beam induced deposition at elevated temperatures: compositional changes and purity improvement *Nanotechnology* **22** 55302
- [15] Utke I, Hoffmann P and Melngailis J 2008 Gas-assisted focused electron beam and ion beam processing and fabrication *J. Vac. Sci. Technol. B* **26** 1197–276
- [16] Folch A, Tejada J, Peters C and Wrighton M 1995 Electron-beam deposition of gold nanostructures in a reactive environment *Appl. Phys. Lett.* **66** 2080–2
- [17] Botman A, Hesselberth M and Mulders J J L 2008 Improving the conductivity of platinum-containing nano-structures created by electron-beam-induced deposition *Microelectron. Eng.* **85** 1139–42
- [18] Wnuk J D, Gorham J M, Rosenberg S G, van Dorp W F, Madey T E, Hagen C W and Fairbrother D H 2010 Electron beam irradiation of dimethyl-(acetylacetonate) gold(III) adsorbed onto solid substrates *J. Appl. Phys.* **107** 54301
- [19] Lukaszcyk T, Schirmer M, Steinrück H-P and Marbach H 2008 Electron-beam-induced deposition in ultrahigh vacuum: lithographic fabrication of clean iron nanostructures *Small* **4** 841–6
- [20] Schardein G, Donev E U and Hastings J T 2011 Electron-beam-induced deposition of gold from aqueous solutions *Nanotechnology* **22** 15301
- [21] Koops H, Kretz J, Rudolph M, Weber M, Dahm G and Lee K 1994 Characterization and application of materials grown by electron-beam-induced deposition *Japan. J. Appl. Phys.* **1** 33 7099–107
- [22] Frabboni S, Gazzadi G C, Felisari L and Spessot A 2006 Fabrication by electron beam induced deposition and transmission electron microscopic characterization of sub-10 nm freestanding Pt nanowires *Appl. Phys. Lett.* **88** 213116
- [23] Langford R M, Wang T-X and Ozkaya D 2007 Reducing the resistivity of electron and ion beam assisted deposited Pt *Microelectron. Eng.* **84** 784–8
- [24] Jenke M G, Lerose D, Niederberger C, Michler J, Christiansen S and Utke I 2011 Toward local growth of individual nanowires on three-dimensional microstructures by using a minimally invasive catalyst templating method *Nano Lett.* **11** 4213–7
- [25] Villamor E, Casanova F, Trompenaars P H F and Mulders J J L 2015 Embedded purification for electron beam induced Pt deposition using MeCpPtMe₃ *Nanotechnology* **26** 95303

- [26] Drouin D, Couture A R, Joly D, Tastet X, Aimez V and Gauvin R 2007 CASINO V2.42—a fast and easy-to-use modeling tool for scanning electron microscopy and microanalysis users *Scanning* **29** 92–101
- [27] Mehendale S, Mulders J J L and Trompenaars P H F 2013 A new sequential EBID process for the creation of pure Pt structures from MeCpPtMe₃ *Nanotechnology* **24** 145303
- [28] Friedli V and Utke I 2009 Optimized molecule supply from nozzle-based gas injection systems for focused electron- and ion-beam induced deposition and etching: simulation and experiment *J. Phys. D: Appl. Phys.* **42** 125305
- [29] National Institute of Standards and Technology (NIST): X-Ray Mass Attenuation Coefficients—Carbon, Graphite <http://physics.nist.gov/PhysRefData/XrayMassCoef/ElemTab/z06.html>